

1 INTRODUCTION

2 Above Earth's atmosphere are the a pair of Van Allen radiation belts, a complex
3 and dynamic plasma environment that affects our technology-driven society. These
4 effects include: a higher radiation dose for astronauts and cosmonauts, higher chance
5 of spacecraft failure due to single event upsets that can lead to catastrophic latchups,
6 degradation of silicon (changing the silicon doping) from an extended radiation dose
7 that can degrade a transistor to the point where it no longer function as a switch,
8 and the degradation of the ozone layer due to the chemical production of NO_X and
9 HO_X molecules. With these effects in mind, it is no surprise that the radiation belts
10 have been extensively studied since their discovery in the 1960s.

11 One natural phenomenon in the radiation belts that has been a topic of interest
12 in the space physics community is wave-particle interactions that, as we will explore
13 throughout this dissertation, can accelerate particles to very high energies (e.g. \approx
14 MeV for electrons) and scatter them into the atmosphere.

15 The goal of this dissertation is to study the wave-particle scattering mechanism
16 that scatters electron microbursts. Electron microbursts, henceforth referred to
17 as microbursts, are typically observed by low Earth orbiting spacecraft, sounding
18 rockets, and high altitude balloons as a sub-second impulse of electrons. Some of
19 the most intense microbursts are observed as a 10 to 100 fold increase of electrons
20 (for example see Fig. 7 in Blake et al. (1996)). Since they were first reported by
21 Anderson and Milton (1964), the short microburst duration and their impulsive nature
22 have compelled countless researchers to understand their properties and the physical
23 mechanism(s) that create microbursts. Microbursts are widely believed to be created
24 by wave-particle scattering between a plasma wave called whistler mode chorus
25 and outer radiation belt electrons, although many details regarding the scattering

²⁶ mechanism are unconstrained or unknown.

²⁷ This chapter serves as an introduction to the physics of charged particles, plasma
²⁸ waves, and the wave-particle interactions in Earth's magnetosphere. We will first
²⁹ derive the motion of individual charged particles in Earth's electric and magnetic
³⁰ fields. Then we will cover how various groups of charged particles coalesce to form
³¹ the major particle populations in the magnetosphere. Then, we will cover the various
³² mechanisms that accelerate particles in the magnetosphere. Lastly, we will review
³³ the basics of microbursts as a jumping-off point for the rest of the dissertation.

³⁴ Charged Particle Motion in Electric and Magnetic Fields

A charged particle trapped in the magnetosphere will experience three types of periodic motion in Earth's nearly dipolar magnetic field. The three motions are ultimately due to the Lorentz force that a particle of momentum \vec{p} , charge q , and velocity \vec{v} experiences in an electric field \vec{E} and magnetic field \vec{B} and is given by

$$\frac{d\vec{p}}{dt} = q(\vec{E} + \vec{v} \times \vec{B}). \quad (1.1)$$

³⁵ In the magnetosphere, the three periodic motions, in decreasing frequency, are
³⁶ gyration, bounce, and drift and are schematically shown in Fig. 1.1. Each of periodic
³⁷ these motions have a corresponding conserved quantity i.e. an adiabatic invariant.

The highest frequency periodic motion is gyration about a magnetic field of magnitude B . This motion is circular with a Larmor radius of

$$r = \frac{mv_{\perp}}{|q|B} \quad (1.2)$$

where m is the mass and v_{\perp} the particle's velocity perpendicular to \vec{B} . This motion

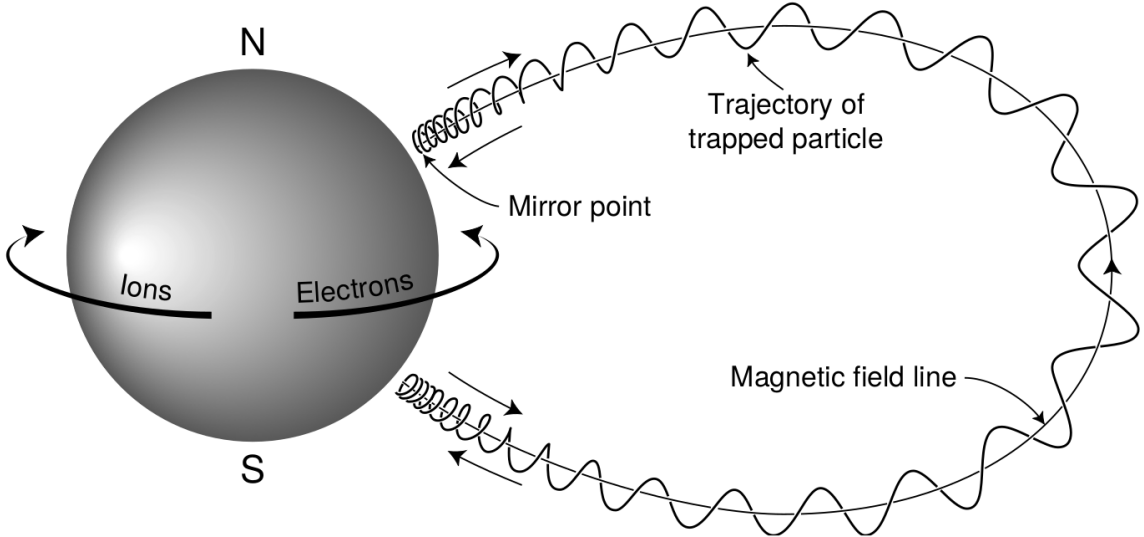


Figure 1.1: The three periodic motions of charged particles in Earth's dipole magnetic field. These motions are: gyration about the magnetic field line, bounce motion between the magnetic poles, and azimuthal drift around the Earth. Figure from (Baumjohann and Treumann, 1997).

has a corresponding gyrofrequency

$$\Omega = \frac{|q|B}{m} \quad (1.3)$$

in units of radians/second. Inside the radiation belts the electron gyrofrequency, Ω_e is on the order of a kHz. The corresponding adiabatic invariant is found by integrating the particle's canonical momentum around the particle's path of gyration

$$J_i = \oint (\vec{p} + q\vec{A}) \cdot d\vec{l} \quad (1.4)$$

³⁸ where J_i is the i^{th} adiabatic invariant and \vec{A} is the magnetic vector potential. This
³⁹ integral is carried out by integrating the first term over the circumference of the gyro
⁴⁰ orbit and integrating the second term using Stokes theorem to calculate the magnetic
⁴¹ flux enclosed by the gyro orbit. The gyration invariant is then $J_1 \sim v_{\perp}^2/B$, which is

⁴² conserved when the frequency, ω of a force acting on the gyrating electron satisfies
⁴³ $\omega \ll \Omega_e$.

⁴⁴ The second highest frequency periodic motion is bouncing due to a parallel
⁴⁵ gradient in \vec{B} . This periodic motion naturally arises in the magnetosphere because
⁴⁶ Earth's magnetic field is stronger near the poles, and artificially in the laboratory
⁴⁷ in magnetic bottle machines. To understand this motion we first we need to define
⁴⁸ the concept of pitch angle α as the angle between \vec{B} and \vec{v} which is schematically
⁴⁹ shown in Fig. 1.2a. The pitch angle relates v with v_{\perp} , and v_{\parallel} (the component of the
⁵⁰ particles velocity parallel to \vec{B}). As shown in 1.2b and c, a smaller (larger) α will
⁵¹ increase (decrease) the distance that the charged particle travels parallel to \vec{B} , during
⁵² one gyration.

Assuming the particle's kinetic energy is conserved, the conservation of J_1 implies that given a particle's $v_{\perp}(0)$ and $B(0)$ at the magnetic equator (where Earth's magnetic field is usually at a minimum), we can calculate its $v_{\perp}(s)$ along the particle's path s by calculating $B(s)$ from magnetic field models. The particle's perpendicular velocity is then related via

$$\frac{v_{\perp}^2(0)}{B(0)} = \frac{v_{\perp}^2(s)}{B(s)} \quad (1.5)$$

⁵³ which can be rewritten as

$$\frac{v^2 \sin^2 \alpha(0)}{B(0)} = \frac{v^2 - v_{\parallel}^2(s)}{B(s)} \quad (1.6)$$

⁵⁴ and re-arranged to solve for $v_{\parallel}(s)$

$$v_{\parallel}(s) = v \sqrt{1 - \frac{B(s)}{B(0)} \sin^2 \alpha(0)} \quad (1.7)$$

⁵⁵ which will tend towards 0 when the second term in the radical approaches 1.

56 The location where $v_{||}(s) = 0$ is called the mirror point and is where a particle
 57 reverses direction. Since Earth's magnetic field is stronger towards the poles, the
 58 mirroring particle will execute periodic bounce motion between its two mirror points
 59 in the northern and southern hemispheres. The corresponding adiabatic invariant, J_2
 60 is

$$J_2 = \oint p_{||} ds \quad (1.8)$$

where ds describes the particle path between the mirror points in the northern and southern hemispheres (see Fig. 1.1). J_2 is found by substituting Eq. 1.7 into Eq. 1.8 and defining the magnetic field strength at the mirror points as B_m where $\alpha(m) = 90^\circ$.

The J_2 integral can be written as

$$J_2 = 2p \int_{m_n}^{m_s} \sqrt{1 - \frac{B(s)}{B(m)}} ds \quad (1.9)$$

61 where m_n and m_s are the northern and southern mirror points, respectively. The
 62 bounce period can be estimated (e.g. Baumjohann and Treumann, 1997) to be

$$t_b \approx \frac{LR_e}{\sqrt{W/m}} (3.7 - 1.6 \sin \alpha(0)) \quad (1.10)$$

63 where L is the L -shell which describes the distance from the Earth's center to the
 64 location where a particular magnetic field line crosses the magnetic equator, in units
 65 of Earth radii, R_e . W is the particle's kinetic energy. As with gyration, the particle
 66 will bounce between the mirror points as long as $\omega \ll \Omega_b$, where Ω_b is the bounce
 67 frequency.

68 At this stage it is instructional to introduce the notion of the loss cone pitch
 69 angle, α_L . A particle with $\alpha \leq \alpha_L$ will mirror at or below ≈ 100 km altitude in

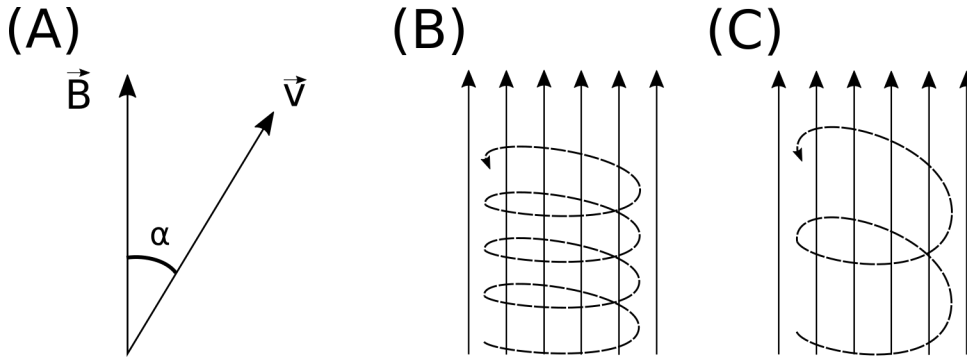


Figure 1.2: Charged particle motion in a uniform magnetic field \vec{B} . Panel (A) shows the geometry defining the pitch angle, α . Panel (B) and (C) show two helical electron trajectories with dashed lines assuming a large and small α (corresponding to a small and large parallel velocity $v_{||}$), respectively.

70 the atmosphere. A charged particle gyrating at those altitudes will encounter and
71 Coulomb scatter with the dense atmosphere and be lost from the magnetosphere.

72 The slowest periodic motion experienced by charged particles in Earth's mag-
73 netic field is azimuthal drift around the Earth. This drift results from a combination of
74 a radial gradient in \vec{B} and the curvature of the magnetic field. The radial gradient drift
75 arises because Earth's magnetic field is stronger near the Earth where the particle's
76 gyroradius radius of curvature is smaller as it gyrates towards stronger magnetic field,
77 and larger when it gyrates outward. The overall effect is the particle gyro orbit does
78 not close on itself and negatively charged particles drift east and positively charged
79 particles drift west. The radial gradient drift is enhanced by the centrifugal force that
80 a particle experiences as it bounces along the curved field lines. The drift adiabatic
81 invariant, J_3 is found by integrating Eq. 1.4 over the complete particle orbit around
82 the Earth. The shape of this drift orbit is otherwise known as a drift shell. For J_3 ,
83 the first term is negligible and the second term is the magnetic flux enclosed by the
84 drift shell, Φ_m i.e. $J_3 \sim \Phi_m$.

85 Figure 1.3 from Schulz and Lanzerotti (1974) shows contours of the gyration,

⁸⁶ bounce, and drift frequencies for electrons and protons in Earth's dipole magnetic
⁸⁷ field.

Up until now we have considered the three periodic motions due Earth's magnetic field and the absence of electric fields. If \vec{E} is present, a particle's center of gyration i.e., averaged position of the particle over a gyration, will drift with a velocity perpendicular to both \vec{E} and \vec{B} . The drift velocity can be solved directly from Eq. 1.1 and is

$$\vec{v}_E = \frac{\vec{E} \times \vec{B}}{B^2}. \quad (1.11)$$

⁸⁸ Lastly, for more detailed derivations of these motions, see the following texts:
⁸⁹ Baumjohann and Treumann (1997); Schulz and Lanzerotti (1974); Tsurutani and
⁹⁰ Lakhina (1997).

⁹¹ Particle Populations and Their Interractions in the Magnetosphere

⁹² Now that we have looked at the dynamics of single-particle motion, we will
⁹³ briefly tour the various macroscopic populations in the magnetosphere. Various
⁹⁴ magnetosphere populations are illustrated in Figs. 1.4 and 1.5. In this section we
⁹⁵ will introduce the various particle populations in the magnetosphere and how they
⁹⁶ couple. **When slimming, remove Fig. 1.4?**

⁹⁷ The sun and its solar wind are ultimately the source of energy input into the
⁹⁸ magnetosphere. The solar wind at Earth's orbit is a plasma traveling at supersonic
⁹⁹ speeds with an embedded interplanetary magnetic field (IMF). When the solar wind
¹⁰⁰ encounters Earth's magnetic field the plasma can not easily penetrate into the
¹⁰¹ magnetosphere, rather it drapes around the magnetosphere forming a cavity in the
¹⁰² solar wind that is roughly shaped as shown in Fig. 1.4. Because the solar wind is
¹⁰³ supersonic at 1 AU, a bow shock exists upstream of the magnetosphere. The solar

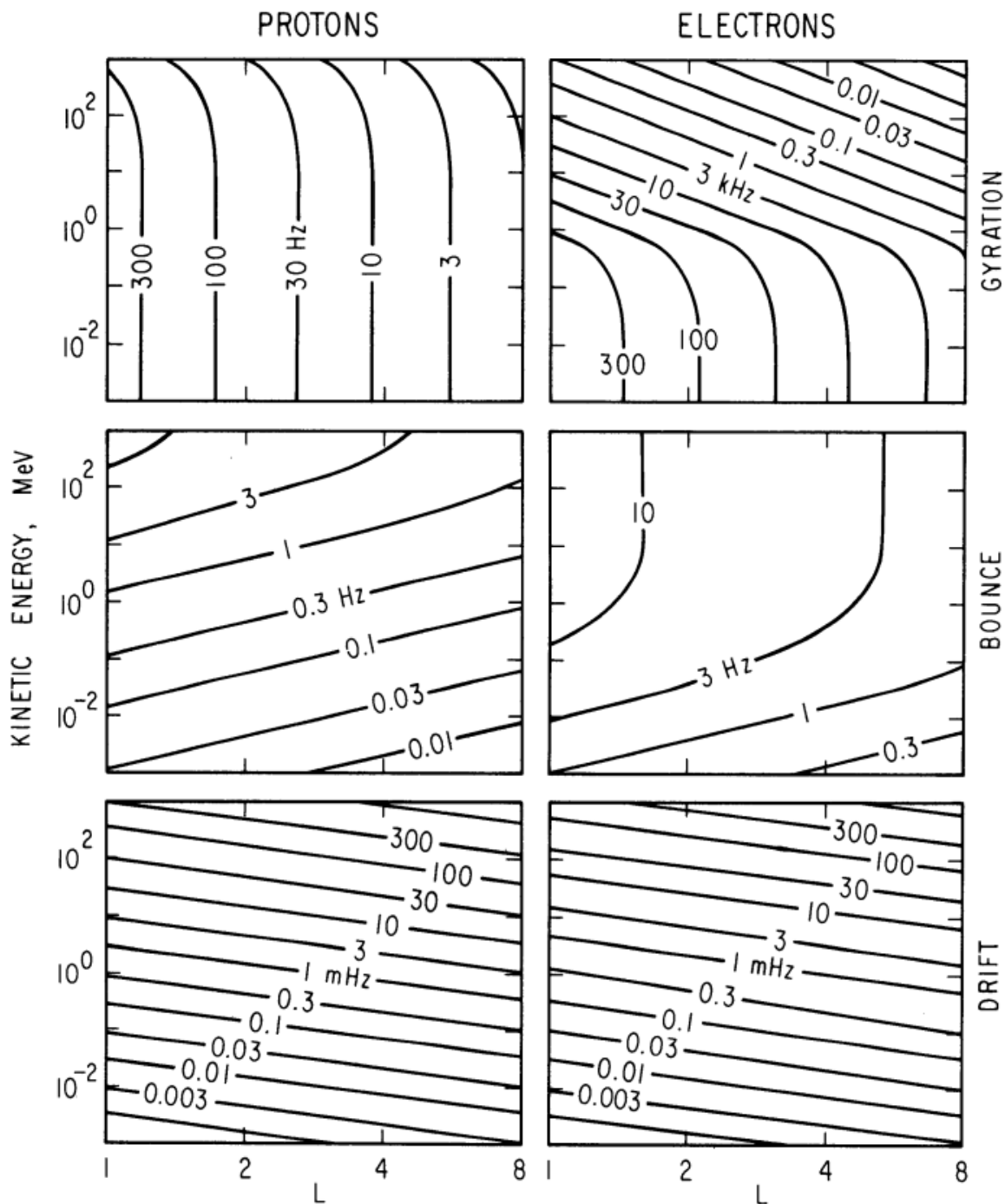


Figure 1.3: Contours of constant gyration, bounce, and drift frequencies for electrons and protons in a dipole field. Figure from Schulz and Lanzerotti (1974).

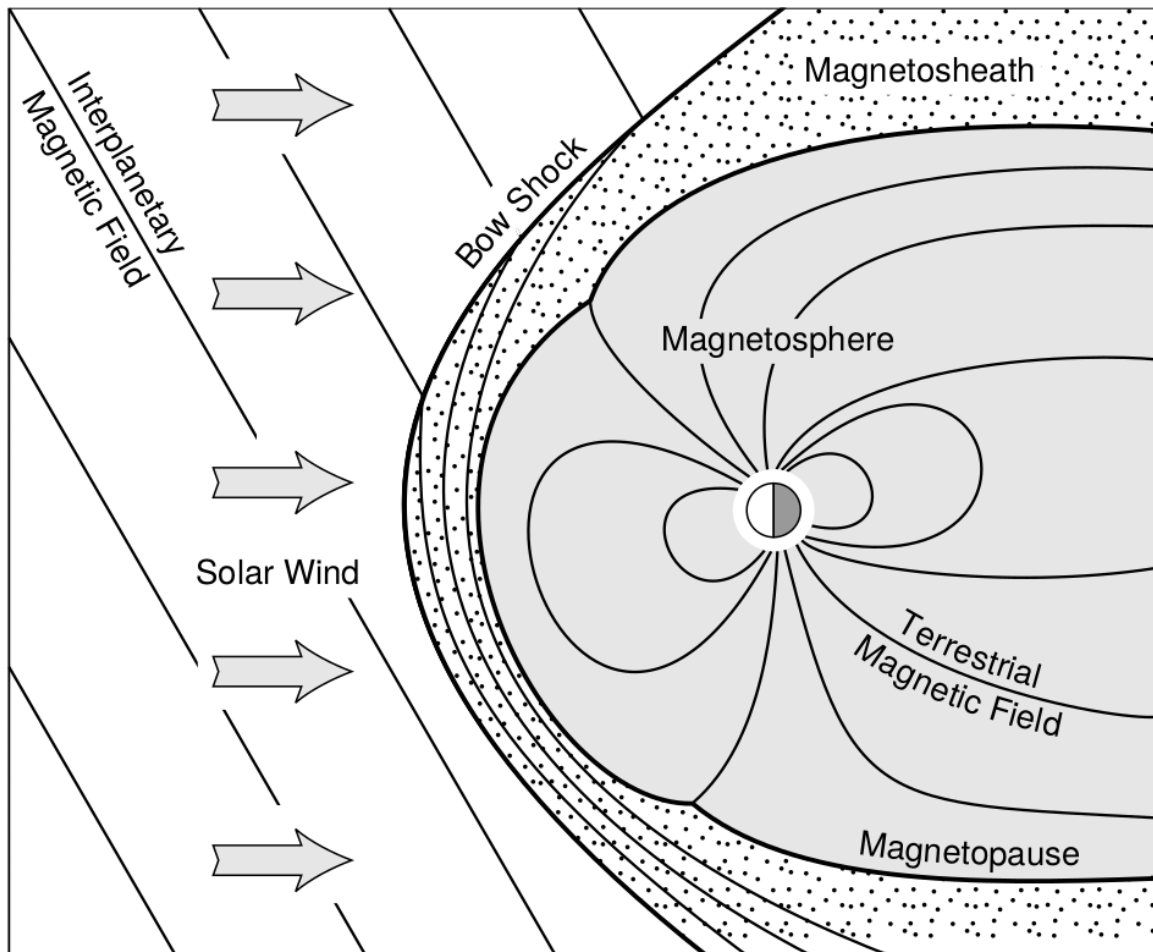


Figure 1.4: Macroscopic structures in the outer magnetosphere. The solar wind with its frozen-in interplanetary magnetic field is shown on the left and is traveling supersonically towards the right. The solar wind envelops Earth's magnetic field to create the magnetosphere cavity. Since the solar wind is traveling supersonically, it creates a bow shock up stream. Downstream of the bow shock the shocked solar wind plasma inside the magnetosheath flows around the magnetopause, a boundary between the solar wind and magnetosphere. Figure from Baumjohann and Treumann (1997).

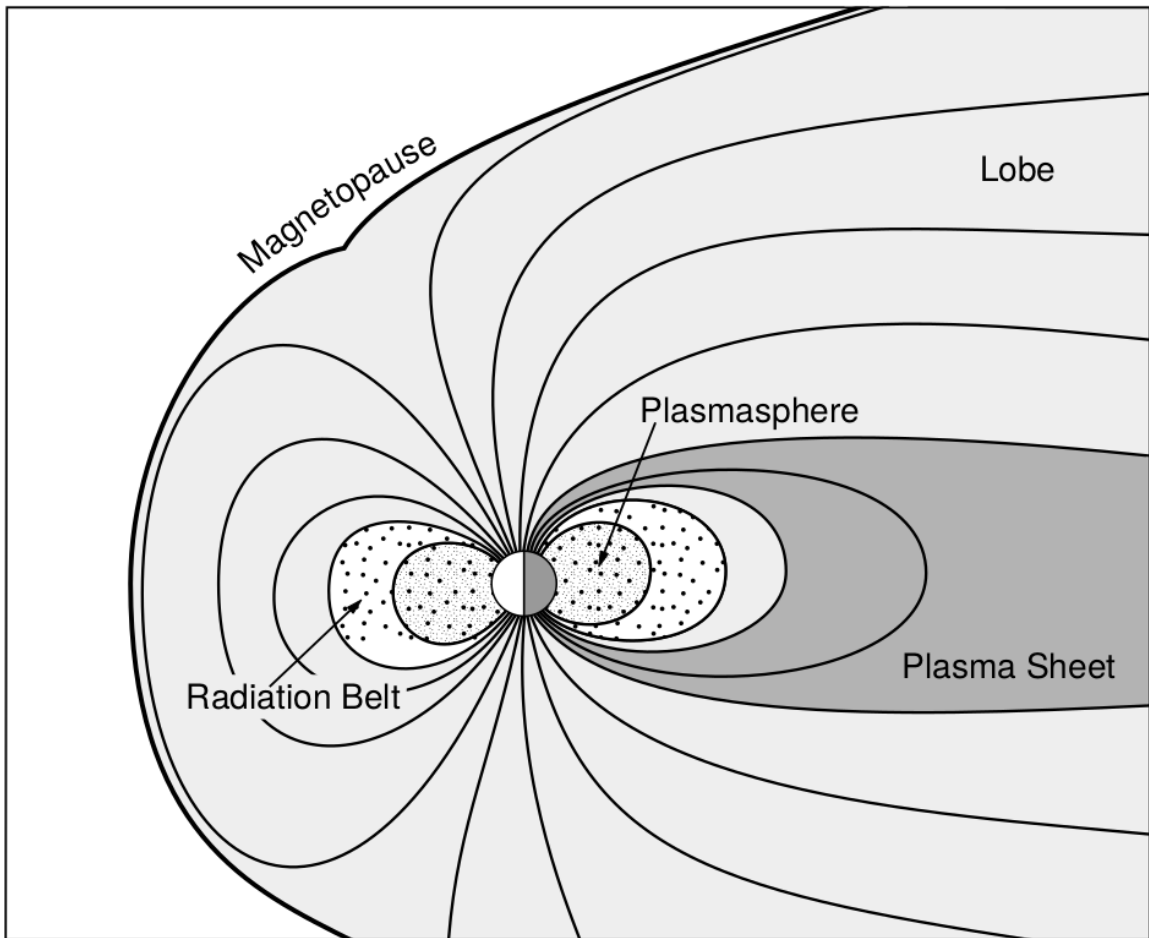


Figure 1.5: Macroscopic structures in the inner magnetosphere most relevant to this dissertation. The plasmasphere, and the radiation belts are shown and ring current is co-located there as well. Sun is to the left. Figure from Baumjohann and Treumann (1997).

wind plasma, after it is shocked by the bow shock, flows around the magnetosphere
 inside the magnetosheath. The surface where the solar wind ram pressure and Earth's
 magnetic pressure balance is termed the magnetopause, which can be thought of as
 a boundary between the solar wind's and Earth's plasma environments. This is
 a slightly naive description of the magnetopause, but is nonetheless an instructive
 conceptual picture. The shocked plasma then flows past the Earth where it shapes
 the magnetotail. In the magnetotail the solar wind magnetic pressure balances Earth's
 magnetic field pressure in the lobes. The magnetotail extends on the order of 100
 R_E downstream of Earth [Add citation](#), and the tailward stretching of magnetic field
 lines creates the plasma sheet which exists in the region of low magnetic field strength
 near the magnetic equator [Add citation](#). The plasma sheet flows from dusk to dawn
 (out of the page in Figs. 1.4 and 1.5) and this current is connected to a zoo of other
 currents in the magnetosphere which is beyond the scope of this dissertation.

The idea of the magnetopause as a barrier between the solar wind and
 the magnetosphere is not entirely accurate due to the presence of reconnection.
 Reconnection was first conceived by Dungey (1961) who described the convection of
 Earth's magnetic field between the bow and tail regions of the magnetosphere. This
 process is known as the Dungey cycle and is most effective when the IMF is pointing
 southward as is shown in Fig. 1.6 part 1. As the IMF contacts Earth's magnetic
 field it reconnects with it so that Earth's magnetic field is directly connected to the
 IMF. Then as the solar wind flows tailward the IMF drags Earth's magnetic field
 towards the magnetotail as shown in Fig. 1.6 parts 2-6. As more and more magnetic
 field lines are draped in the magnetotail, magnetic pressure increases in the lobes
 which squeezes the plasma sheet until Earth's magnetic field reconnects as is shown
 in Fig. 1.6 part 7. Lastly, Fig. 1.6 part 8 shows the newly merged magnetic field
 line and the plasma frozen on it moves Earthward under the magnetic tension force

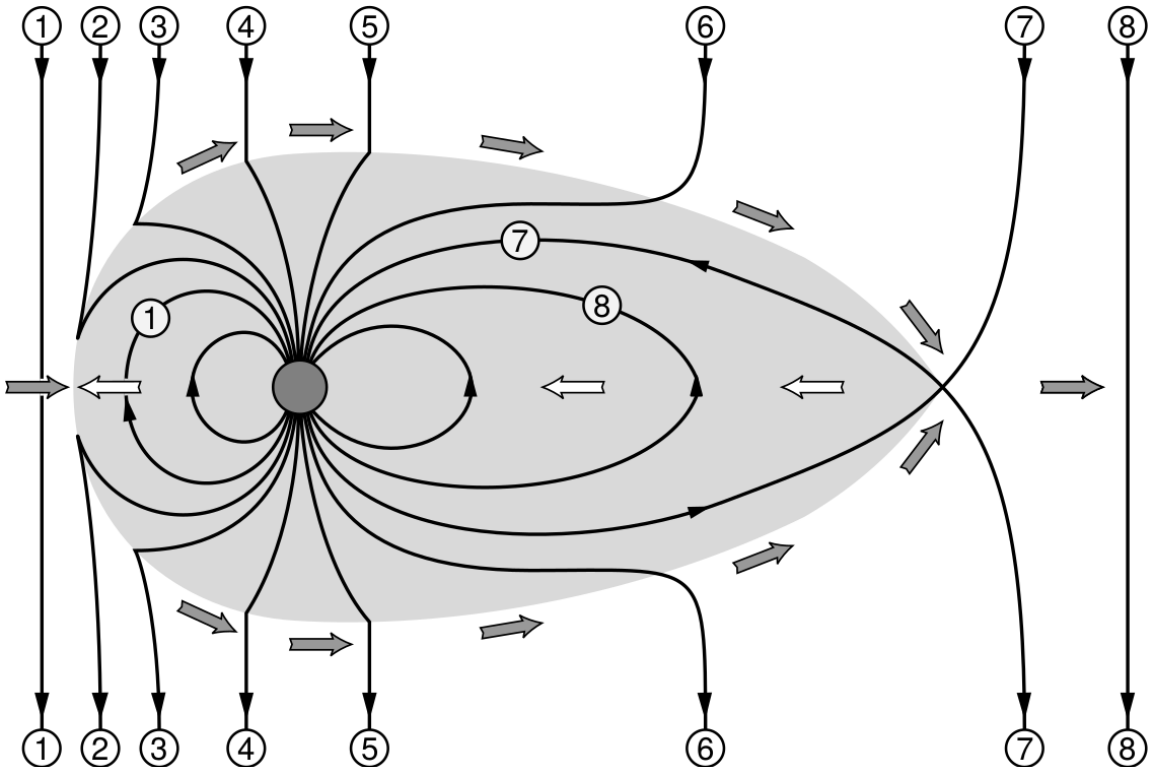


Figure 1.6: The series of steps involved in magnetic reconnection with a southward IMF. Figure from Baumjohann and Treumann (1997).

to become more dipolar. This is called a dipolarization of the magnetic field, and the plasma frozen on these field lines can be observed as injections (e.g. Turner et al., 2015). Injection of plasma into the inner magnetosphere is one of the drivers of inner magnetosphere dynamics. Should I talk about the K-H instability and how there could be micro reconnection? i.e. cite a paper or two that support or refute that idea.

136 Inner Magnetosphere Populations

Before we describe the inner magnetosphere particle populations, we first need to describe the coordinate system used to organize the inner magnetosphere populations. The first coordinate was defined in section 1 and is the L shell. L shell can be thought

140 of as an analogue to a radius but in a dipole geometry. The azimuthal coordinate
 141 is the magnetic local time (MLT). For an observer above Earth's north pole looking
 142 down, MLT is defined to be 0 (midnight) in the anti-sunward direction, and increases
 143 in the counter-clockwise direction with 6 at dawn, 12 at noon (sunward direction),
 144 and 18 in dusk. The last coordinate used in this dissertation is the magnetic latitude,
 145 λ which is analogous to the latitude coordinate and is defined to be 0 at the magnetic
 146 equator.

147 The low energy particle dynamics in the inner magnetosphere are organized by
 148 two electric fields: the co-rotation and the dawn-dusk electric fields. The co-rotation
 149 electric field arises from the rotation of Earth's magnetic field. Since particles are
 150 frozen on magnetic field lines and the plasma conductivity is effectively infinite, to
 151 a non-rotating observer, Earth's rotation appears as a radial electric field that drops
 152 off as $\sim L^2$. This electric field makes particles orbit around the Earth due to the
 153 $\vec{E} \times \vec{B}$ drift. The other electric field, pointing from dawn to dusk is called the
 154 convection electric field and is formed by the Earthward transport of particles from
 155 the magnetotail that appears as an electric field to a stationary observer (with respect
 156 to Earth). The superposition of the co-rotation and convection electric fields
 157 results in a potential field shown in Fig. 1.7. The shaded area in Fig. 1.7 shows
 158 the orbits on which low energy electrons are trapped, and outside are the untrapped
 159 particles. The dynamic topology of the shaded region in Fig. 1.7 is controlled by only
 160 the convection electric field which is dependent on the solar wind speed and the IMF.
 161 The lowest energy particles, that are most effected by these electric fields, make up
 162 the plasmasphere.

163 Plasmasphere The plasmasphere is a dense ($n_e \sim 10^3/\text{cm}^3$), cool plasma
 164 ($\sim \text{eV}$) that extends to $L \sim 4$ (extent is highly dependent on the solar wind and

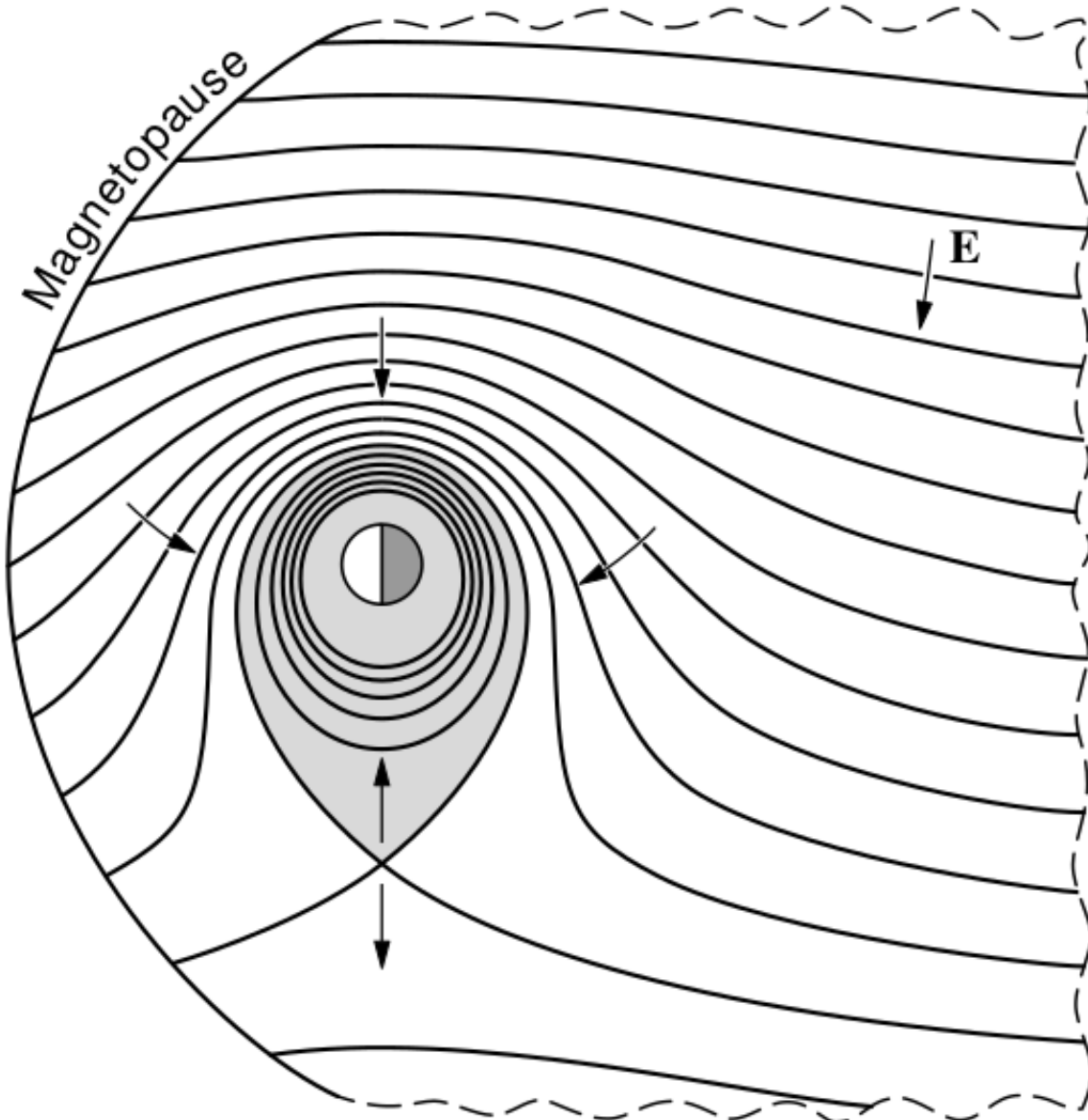


Figure 1.7: Equipotential lines and electric field arrows due to the superposition of the co-rotation and convection electric fields. Electrons in the shaded region execute closed orbits. Outside of the shaded regions the electrons are not trapped and will escape. The region separating the two regimes is called the Alfvén layer. Figure from Baumjohann and Treumann (1997).

165 magnetospheric conditions) and is sourced from the ionosphere. The two main
 166 mechanisms that source the cold plasma from the ionosphere are ultraviolet ionization
 167 by sunlight and particle precipitation. The ultraviolet ionization by sunlight is
 168 strongly dependent on the time of day (day vs night), latitude (more ionization near
 169 the equator). The ionization due to particle precipitation, on the other hand, is highly
 170 dependent on magnetospheric conditions, and mostly occurs at high latitudes.

171 The outer boundary of the plasmasphere is the plasmapause which is typically
 172 identified as a steep radial gradient in plasma density from $\sim 10^3/\text{cm}^3$ to $\sim 1/\text{cm}^3$. As
 173 we will see throughout this dissertation, the location of the plasmapause is important
 174 to model (e.g. O'Brien and Moldwin, 2003) and understand since the plasma density
 175 strongly controls the efficiency of particle scattering (Horne et al., 2005).

176 Ring Current The next higher energy population is the ring current. This
 177 population consists of protons and electrons between tens and a few hundred keV
 178 that drift around the Earth. The orbits of higher energy particles are not as effected
 179 by the convection and co-rotation electric field, rather they drift around the Earth
 180 due to gradient and curvature drifts. Since the direction of the drift is dependent on
 181 charge, protons drift west around the Earth and electrons drift East. This has the
 182 effect of creating a current around the Earth.

183 The ring current generates a magnetic field which decreases the magnetic field
 184 strength on Earth's surface and increases it outside of the ring current. The decrease
 185 of Earth's magnetic field strength is readily observed by a system of ground-based
 186 magnetometers and is merged into a Disturbance Storm Time (DST) index. An
 187 example of a DST index time series from a coronal mass ejection (CME) driven 2015
 188 St. Patrick's Day storm is shown in Fig. 1.8. The ring current is sometimes first
 189 depleted and DST increases slightly (initial phase or sudden storm commencement).

190 Then the ring current is rapidly built up during which DST rapidly decreases (main
 191 phase). Lastly the ring current gradually decays toward its equilibrium state over a
 192 period of a few days and DST increases towards 0 (recovery phase). The DST index
 193 along with other indices are readily used by the space physics community to quantify
 194 the global state of the magnetosphere.

195 Radiation Belts The highest energy particle populations are in the Van Allen
 196 radiation belts. These belts were discovered by Van Allen (1959) and Vernov and
 197 Chudakov (1960) during the Cold War and are a pair of toroidally shaped populations
 198 of trapped electrons and protons usually within to $L < 8$ and are shown in Fig. 1.9.
 199 Their quiescent toroidal shape is similar to the shape of the plasmasphere and ring
 200 current and is a result of Earth's dipole magnetic field and the conservation of the
 201 three adiabatic invariants discussed in section 1.

202 The inner radiation belt is extremely stable on time periods of years, extends
 203 to $L \approx 2$, and mainly consists of protons with energies between MeV and GeV and
 204 electrons with energies up to ≈ 1 MeV (Claudepierre et al., 2019). The source of
 205 inner radiation belt protons is believed to be due to cosmic-ray albedo neutron decay
 206 (e.g. Li et al., 2017) and inward radial diffusion for electrons (e.g. O'Brien et al.,
 207 2016). The gap between the inner and outer radiation belt is called the slot, which is
 208 believed to be due to hiss waves inside the plasmasphere (described below) scattering
 209 particles into the atmosphere (e.g. Breneman et al., 2015; Lyons and Thorne, 1973).

210 The outer radiation belt, on the other hand is much more dynamic and consists
 211 of mainly electrons of energies up to a few MeV. The outer belt's spatial extent is
 212 highly variable e.g. see Fig. 1.10, and is typically observed at $4 < L < 8$. Since
 213 the outer radiation belt contains a dynamic population of energetic particles that
 214 pose a threat to human and technological presence in Earth's atmosphere and space,

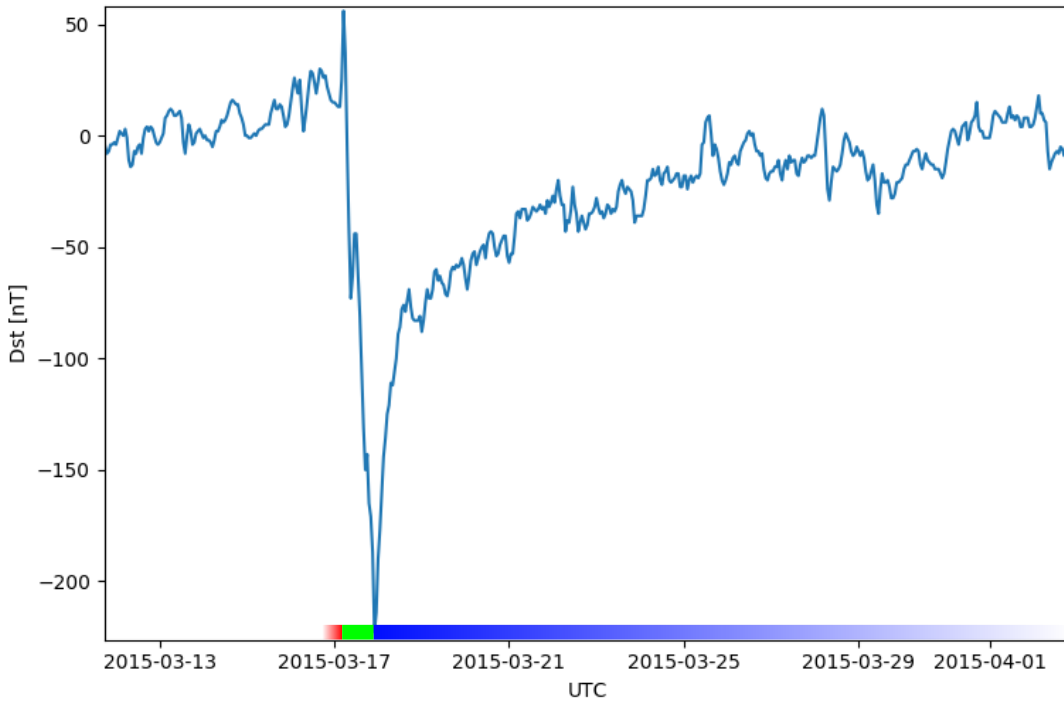


Figure 1.8: The DST index during the St. Patrick's Day 2015 storm. This storm was caused by a coronal mass ejection on March 15th, 2015. The storm phases are: initial phase, main phase, and recovery phase. The initial phase occurred when the Dst peaked at +50 nT on March 17th during which the ring current was eroded by the coronal mass ejection during the interval shown by the red bar. Then the rapid decrease to ≈ -200 nT was during the main phase where many injections from the magnetotail pumped up the ring current which reduced Earth's magnetic field strength at the ground and is shown with the green bar. Lastly, the recovery phase lasted from March 18th to approximately March 29th during which the ring current particles were lost and the ring current returned to its equilibrium state. The recovery phase is shown with the blue bar.

The Earth's Electron Radiation Belts

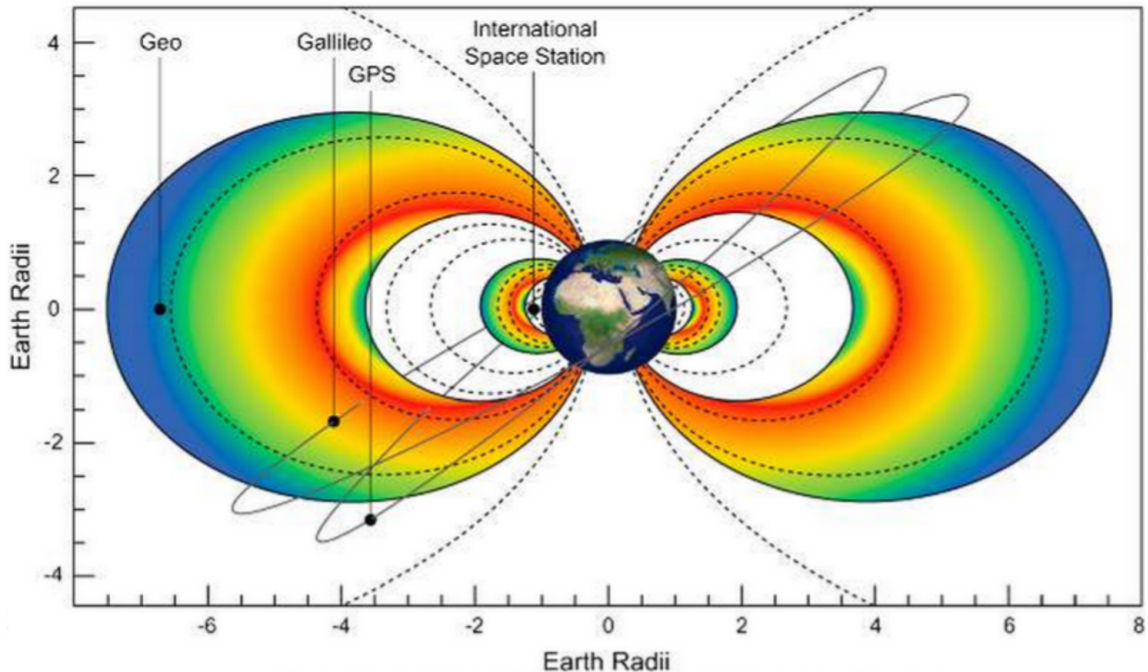


Figure 1.9: The two radiation belts with the locations of various satellites and orbits.
Figure from (Horne et al., 2013).

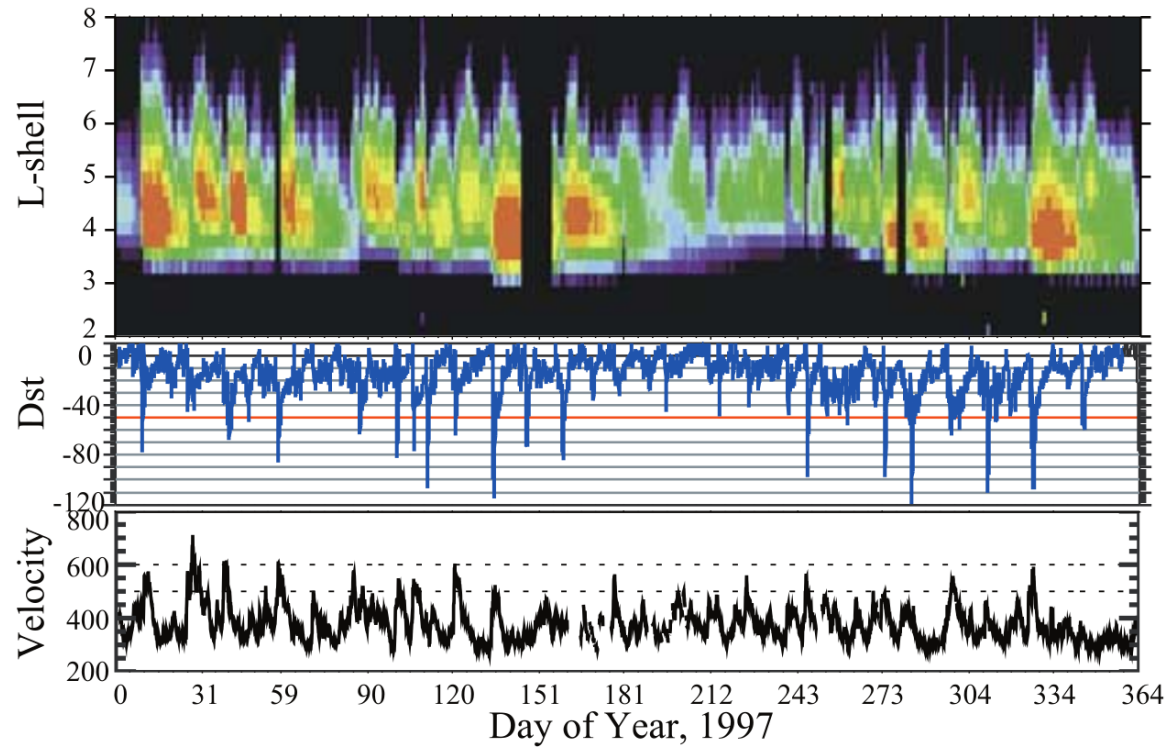


Figure 1.10: The dynamics of the outer radiation belt in 1997 from the POLAR satellite. Top panel shows the 1.2-2.4 MeV electron flux as a function of L and 1997 day of year. The middle panel shows the DST index, and bottom panel shows the solar wind velocity. Figure from (Reeves et al., 2003).

215 decades of research has been undertaken to understand and predict the outer radiation
 216 belt particles, waves, and wave-particle interactions. The dynamics of the outer
 217 radiation belt can be understood by considering various competing acceleration and
 218 loss mechanisms which will be described in the following sections.

219

Radiation Belt Particle Sources and Sinks

220 Adiabatic Heating

221 One of the particle heating and transport mechanisms arises from the Earthward
 222 convection of particles. The conservation of J_1 implies that the initial and final v_\perp
 223 depends on the change in the magnetic field amplitude

$$\frac{v_{\perp i}^2}{B_i} = \frac{v_{\perp f}^2}{B_f}. \quad (1.12)$$

224 As a particle convects Earthward, $B_f > B_i$ thus v_\perp must increase. The dipole
 225 magnetic field amplitude can be written as

$$B(L, \theta) = \frac{31.2 \mu\text{T}}{L^3} \sqrt{1 + 3 \cos^2 \theta} \quad (1.13)$$

226 which implies that

$$\frac{v_{\perp f}^2}{v_{\perp i}^2} = \left(\frac{L_i}{L_f} \right)^3. \quad (1.14)$$

227 .

228 In addition, as the particle convects Earthward the distance between the
 229 particle's mirror points decrease. If J_2 is conserved, the shrinking bounce path implies

²³⁰ that v_{\parallel} must increase by

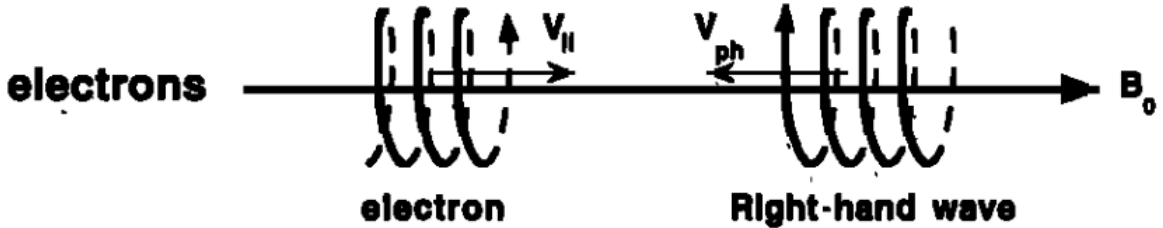
$$\frac{v_{\parallel f}^2}{v_{\parallel i}^2} = \left(\frac{L_i}{L_f} \right)^k \quad (1.15)$$

²³¹ where k ranges from 2 for equatorial pitch angles, $\alpha_{eq} = 0^\circ$, to 2.5 for $\alpha_{eq} = 90^\circ$
²³² (Baumjohann and Treumann, 1997). Since the rate of adiabatic heating is greater in
²³³ the perpendicular direction than heating in the parallel direction, an initially isotropic
²³⁴ particle distribution will become anisotropic during its convection. These isotropic
²³⁵ particles can then become unstable to wave growth and generate waves in order to
²³⁶ reach equilibrium.

²³⁷ Wave Resonance Heating

²³⁸ Another mechanism that heats particles is due to particles resonating with
²³⁹ plasma waves. A few of the electromagnetic wave modes responsible for particle
²⁴⁰ acceleration (and deceleration) relevant to radiation belt dynamics are hiss, whistler
²⁴¹ mode chorus (chorus), and electromagnetic ion cyclotron (EMIC) waves. These waves
²⁴² are created by the loss cone instability that driven by an anisotropy of electrons
²⁴³ for chorus waves, and protons for EMIC waves. The level of anisotropy can be
²⁴⁴ quantified by the ratio of the perpendicular to parallel particle temperatures (T_{\perp}/T_{\parallel}).
²⁴⁵ A particle distribution is unstable when $T_{\perp}/T_{\parallel} > 1$ which facilitates wave growth.
²⁴⁶ Since electrons gyrate in a right-handed sense, the chorus waves also tend to be right
²⁴⁷ hand circularly polarized (Tsurutani and Lakhina, 1997). The same argument applies
²⁴⁸ to protons and left hand circularly polarized EMIC waves as well.

²⁴⁹ These circularly polarized waves can resonate with electrons and/or protons
²⁵⁰ when their combined motion results in a static \vec{E} . One example of a resonance
²⁵¹ between a right hand circularly polarized wave and an electron is shown in Fig. 1.21
²⁵² and is termed the cyclotron resonance. An electron's v_{\parallel} and the wave's parallel wave



$$\omega + k_{\parallel} v_{\parallel} = \Omega^-$$

Figure 1.11: The trajectories of an electron and a right-hand circularly polarized wave during a cyclotron resonance. The electron's v_{\parallel} and the wave's k_{\parallel} are in opposite directions such that the wave's frequency ω is Doppler shifted to an integer multiple of the electron cyclotron frequency. Figure from (Tsurutani and Lakhina, 1997).

vector, k_{\parallel} are in opposite directions such that the wave frequency ω is Doppler shifted to an integer multiple of the Ω_e at which point the electron feels a static electric field and is accelerated or decelerated. This acceleration happens when a resonance condition is satisfied between a wave and a particle for which we will now derive an illustrative toy model.

Assume a uniform magnetic field $\vec{B} = B_0 \hat{z}$ with a parallel propagating ($k = k \hat{z}$), right-hand circularly polarized wave. The wave's electric field as a function of position and time can be written as

$$\vec{E} = E_0 (\cos(\omega t - kz) \hat{x} + \sin(\omega t - kz) \hat{y}) \quad (1.16)$$

which is more clearly expressed by taking the dot product to find \vec{E} in the $\hat{\theta}$ direction

$$E_{\theta} = \vec{E} \times \hat{\theta} = E_0 \cos(\omega t - kz + \theta). \quad (1.17)$$

Now assume that the electron is traveling in the $-\hat{z}$ direction with a velocity $\vec{v} = -v_0 \hat{z}$

²⁶² so its time dependent position along \hat{z} is

$$z(t) = -v_0 t \quad (1.18)$$

²⁶³ and gyrophase is

$$\theta(t) = -\Omega t + \theta(0) \quad (1.19)$$

²⁶⁴ where the first negative sign comes from the electron's negative charge. Now we put
²⁶⁵ this all together and express the electric field and the force that the electron will
²⁶⁶ experience

$$m \frac{dv_\theta}{dt} = qE_\theta = qE_0 \sin((\omega + kv_0 - \Omega)t + \theta(0)). \quad (1.20)$$

²⁶⁷ This is a relatively complex expression, but when the time dependent component,

$$\omega + kv_0 - \Omega = 0, \quad (1.21)$$

²⁶⁸ the electron will be in a static electric field which will accelerate or decelerate the
²⁶⁹ electron depending on θ_0 , the phase between the wave and the electron. **Show Bortnik
²⁷⁰ 2008 plot?** The expression in Eq. 1.21 is commonly referred to as the resonance
²⁷¹ condition and is more generally written as

$$\omega - k_{||}v_{||} = \frac{n\Omega_e}{\gamma} \quad (1.22)$$

²⁷² where n is the resonance order, and γ is the relativistic correction (e.g. Millan and
²⁷³ Thorne, 2007). In the case of the cyclotron resonance, $\omega \approx \Omega_e$ thus J_1 is violated.
²⁷⁴ Since J_1 is violated, J_2 and J_3 are also violated since the conditions required to
²⁷⁵ violate J_2 and J_3 are less stringent than J_1 . It is important to remember that along

276 the particle's orbit it will encounter and experience the effects of many waves along
 277 its orbit. The typical MLT extent of a handful of waves that are capable of resonating
 278 with radiation belt electrons are shown in Fig. 1.12.

279 Particle Losses

280 Now that we have seen two general mechanisms with which particles are
 281 accelerated and transported in the magnetosphere, we will now consider a few
 282 specific mechanisms with which particles are lost to the atmosphere or the solar
 283 wind. One particle loss mechanism into the solar wind is magnetopause shadowing
 284 (e.g. Ukhorskiy et al., 2006). Particles are sometimes lost when the ring current is
 285 strengthened and Earth's magnetic field strength is increased outside of the ring
 286 current (and reduced on Earth's surface). If the time scale of the ring current
 287 strengthening is slower than a particle drift, J_3 is conserved. Then in order to
 288 conserve J_3 while the magnetic field strength is increased, the particle's drift shell
 289 must move outward to conserve the magnetic flux contained by the drift shell. Then
 290 if the particle's drift shell expands to the point that it crosses the magnetopause, the
 291 particle will be lost to the solar wind.

292 **Move to acceleration?** Another particle loss and acceleration mechanism is driven
 293 by ultra low frequency (ULF) waves and is called radial diffusion. Radial diffusion is
 294 the transport of particles from high to low phase space density, f . If the transport is
 295 radially inward, particles will appear to be accelerated. On the other hand, radially
 296 outward radial diffusion can transport particles through the magnetopause where
 297 they will be lost to the solar wind. Reeves et al. (2013) investigated the driver of
 298 particle acceleration during the October 2012 storm and observationally found that
 299 inward radial diffusion was not dominant, rather local acceleration via wave-resonance
 300 heating (i.e. particle diffusion in pitch angle and energy which will be described below)

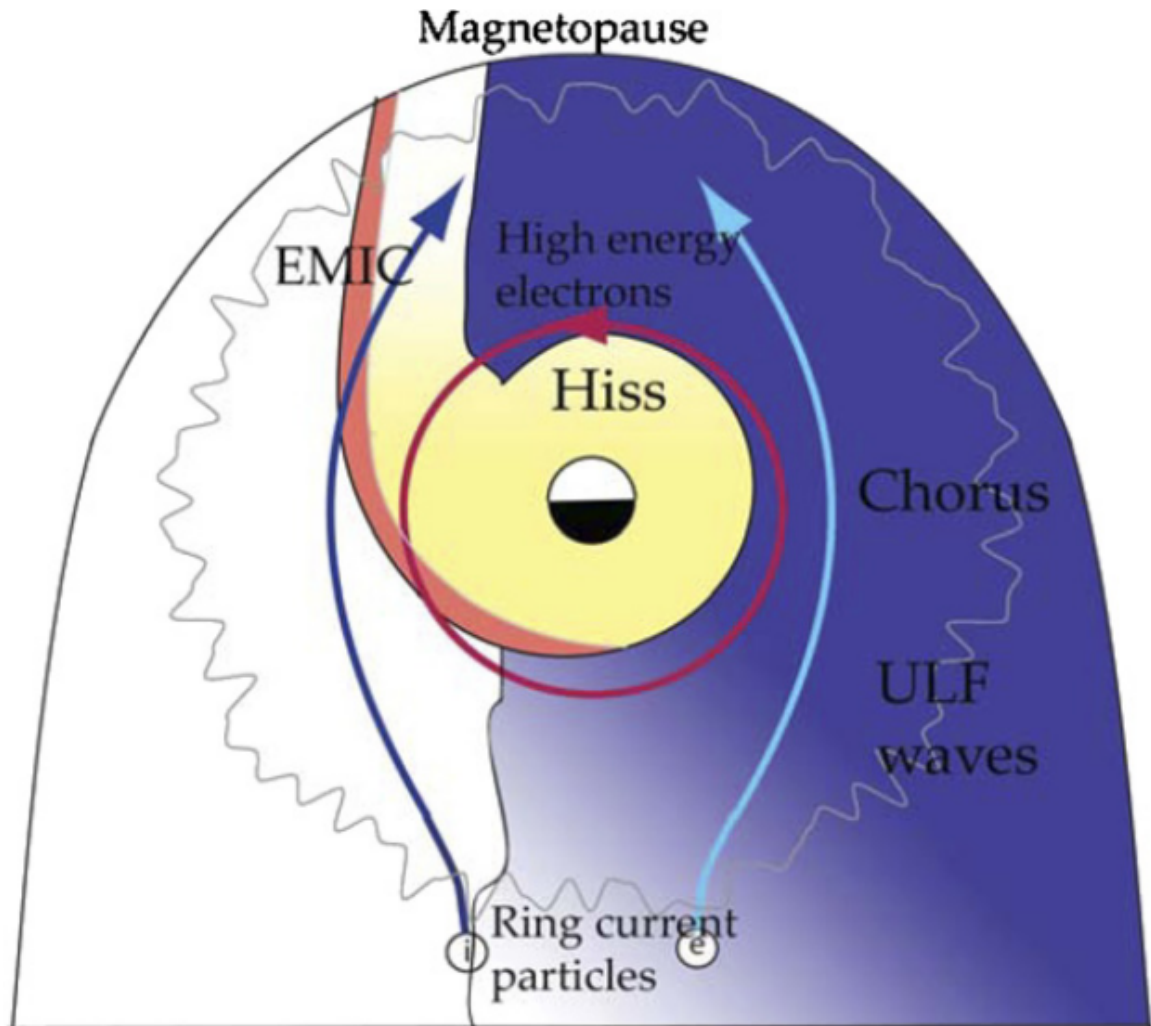


Figure 1.12: Various wave modes in the magnetosphere. Ultra low frequency waves occur through the magnetosphere. Chorus waves are typically observed in the 0-12 midnight-dawn region. EMIC waves are typically observed in the dusk MLT sector. Hiss waves are observed inside the plasmasphere. Figure from Millan and Thorne (2007).

³⁰¹ appeared to be the dominant acceleration mechanism.

³⁰² The loss mechanism central to this dissertation is pitch angle and energy
³⁰³ scattering of electrons by waves. Some of the waves that scatter electrons in energy
³⁰⁴ and pitch angle in the inner magnetosphere are: plasmaspheric hiss (e.g. Breneman
³⁰⁵ et al., 2015; O'Brien et al., 2014), EMIC waves (e.g. Capannolo et al., 2019; Hendry
³⁰⁶ et al., 2017), and chorus waves (e.g. Breneman et al., 2017; Kasahara et al., 2018;
³⁰⁷ Ozaki et al., 2019). These wave-particle interactions occur when the resonance
³⁰⁸ condition in Eq. 1.22 is satisfied at which point the particle's energy and α is modified
³⁰⁹ by the wave. More details regarding the theory of pitch angle and energy diffusion is
³¹⁰ given in Chapter X. If the wave changes α towards 0 such that $\alpha < \alpha_{LC}$, the particle's
³¹¹ mirror point lowers to less than 100 km altitude where the particle can be lost due
³¹² collisions with air. One manifestation of pitch angle scattering of particles into the
³¹³ loss cone are microbursts: a sub-second durtaison impulse of electrons.

³¹⁴

Microbursts

³¹⁵ Microbursts were first identified in high altitude balloon observations of bremsstrahlung
³¹⁶ X-rays emitted by microburst electrons impacting the atmosphere by Anderson and
³¹⁷ Milton (1964). Since then, other balloons have observed microburst X-ray signatures
³¹⁸ in the upper atmosphere (e.g. Anderson et al., 2017; Barcus et al., 1966; Brown et al.,
³¹⁹ 1965; Parks, 1967; Trefall et al., 1966; Woodger et al., 2015). In addition to their X-ray
³²⁰ signature, microbursts electrons have been directly observed in LEO with spacecraft
³²¹ including the Solar Anomalous and Magnetospheric Particle Explorer (SAMPEX),
³²² Focused Investigation of Relativistic Electron Bursts: Intensity, Range, and Dynamics
³²³ II (FIREBIRD-II), Science Technologies Satellite (STSAT-I) (e.g. Blake et al., 1996;
³²⁴ Blum et al., 2015; Breneman et al., 2017; Crew et al., 2016; Lee et al., 2012, 2005;
³²⁵ Lorentzen et al., 2001a,b; Nakamura et al., 1995, 2000; O'Brien et al., 2004, 2003).

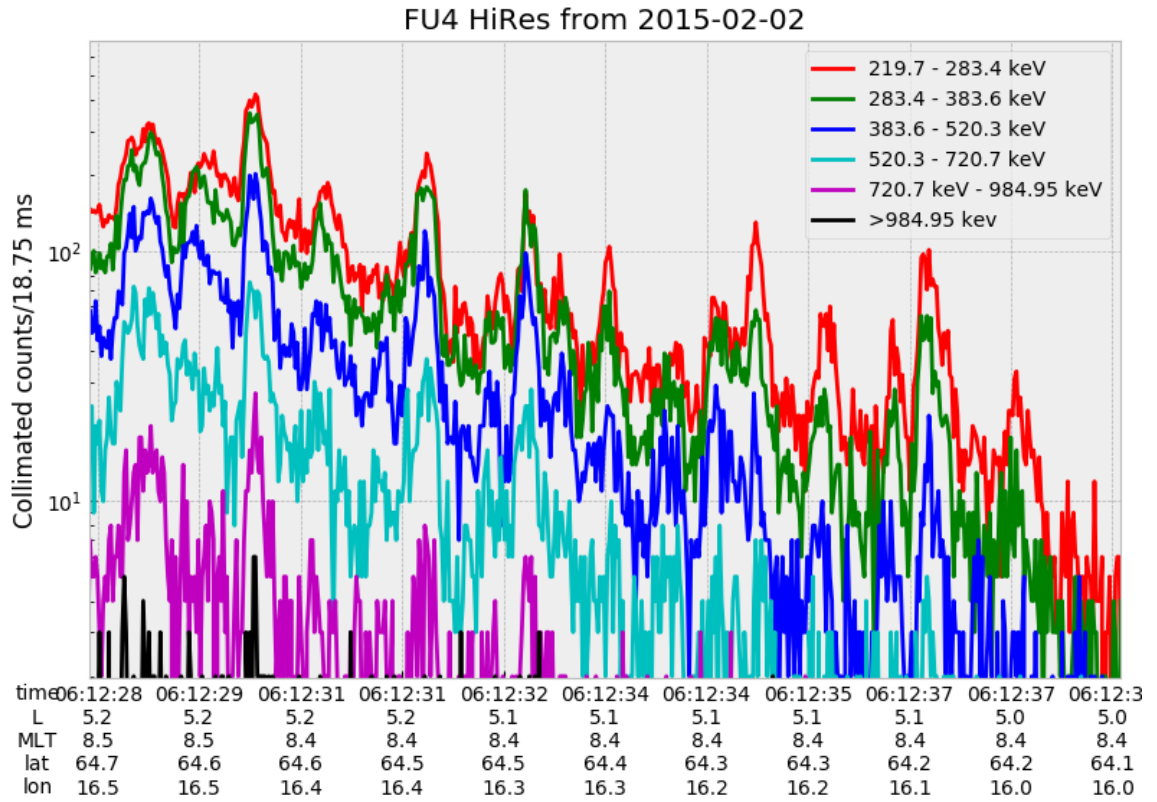


Figure 1.13: An example train of microbursts observed by FIREBIRD-II unit 4 on February 2nd, 2015. The colored curves show the differential energy channel count rates in six channels from ≈ 200 keV to greater than 1 MeV. The x-axis labels show auxiliary information such as time of observation and the spacecraft position in L, MLT, latitude and longitude coordinates.

326 An example microburst time series is shown in Fig. 1.13 and was observed by
 327 Montana State University's (MSU) FIREBIRD-II CubeSats. The prominent features
 328 of microbursts in Fig. 1.13 are their ± 1 second duration, half order of magnitude
 329 increase in count rate above the falling background, and their approximately 200-800
 330 keV energy extent.

331 Microbursts are observed on magnetic field footprints that are connected to the
 332 outer radiation belt (approximately $4 < L < 8$), and are predominately observed in

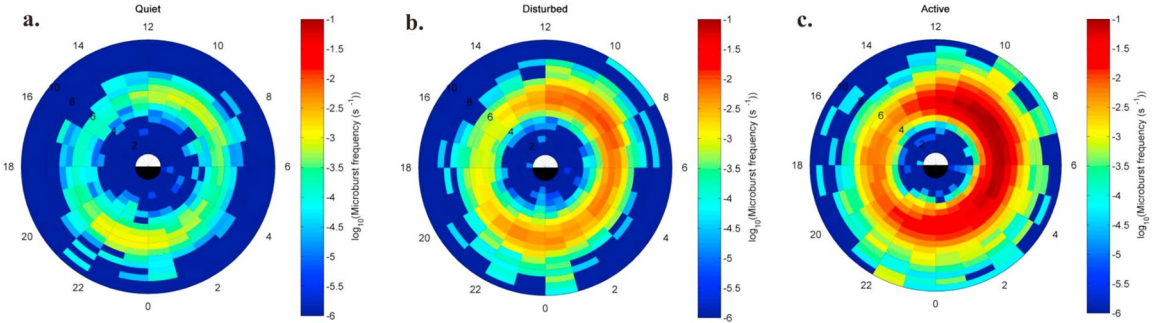


Figure 1.14: Relativistic ($> 1\text{MeV}$) distribution of microburst occurrence rates as a function of L and MLT. The three panels show the microburst occurrence rate dependence on geomagnetic activity, parameterized by the auroral electrojet (AE) index for (a) $\text{AE} < 100 \text{ nT}$, (b) $100 < \text{AE} < 300 \text{ nT}$ and (c) $\text{AE} > 300 \text{ nT}$. Figure from Douma et al. (2017).

333 the 0-12 MLT sector with an elevated occurrence frequency during magnetospherically
 334 disturbed times as shown in Fig. 1.14. Microbursts have been previously observed
 335 over a wide energy range from a few tens of keV (Datta et al., 1997; Parks, 1967) to
 336 greater than 1 MeV (e.g. Blake et al., 1996; Greeley et al., 2019). The microburst
 337 electron flux (J) falls off in energy, and the microburst energy spectra is typically
 338 well fit to a decaying exponential

$$J(E) = J_0 e^{-E/E_0} \quad (1.23)$$

339 where J_0 is the flux at 0 keV (unphysical free parameter) and E_0 quantifies the
 340 efficiency of the scattering mechanism in energy (.e.g Datta et al., 1997; Lee et al.,
 341 2005; Parks, 1967). A small E_0 suggests that mostly low energy particles are scattered
 342 and a high E_0 suggests that the scattering mechanism scatters low and high energy
 343 electrons. Reality is a bit more messy and a high E_0 may be a signature of a scattering
 344 mechanism preferential to high energy electrons, but is hidden by the convolution of
 345 the source particles available to be scattered (typically with a falling energy spectrum)

346 and the energy-dependent scattering efficiency.

347 The short duration of microbursts observed by a single LEO satellite has an
348 ambiguity when interpreting what is exactly a microburst. The two possible realities
349 are: a microburst is very small and spatially stationary so that the LEO spacecraft
350 passes through it in less than a second. Alternatively, microbursts are spatially large
351 with a short duration such that the microburst passes by the spacecraft in a fraction
352 of a second. There are a few ways to distinguish between the two possible realities,
353 and each one has a unique set of advantages.

354 A high altitude balloon provides essentially a stationary view of the precipitating
355 particles under the radiation belt footprints so a short-lived, temporal microburst
356 can be unambiguously identified. Spatial structures on the other hand are difficult
357 to identify because a balloon is essentially still on drift timescales thus a variation in
358 the X-rays can be due to the spatial structure or an increase of precipitating particles
359 over the whole area. Furthermore, if the stationary structure is drifting its particles
360 are not precipitating into the atmosphere so there is no X-ray signature.

361 Another solution is multi-spacecraft missions that can determine if a microburst
362 is spatial or temporal. As will be shown in this dissertation, if a microburst is
363 observed simultaneously by two spacecraft then it is temporally transient and has
364 a size greater than the spacecraft separation. On the other hand, if two spacecraft
365 observe a microburst-like feature in the same location and at different times, then it is
366 spatial may be a curtain (Blake and O'Brien, 2016). Both observational methods have
367 a unique set of strengths, and this dissertation takes the multi-spacecraft approach
368 to identify and study microbursts.

369

Scope of Reserach

370 This dissertation furthers our understanding of the microburst scattering
371 mechanism by observing the scattering directly, and measuring the microburst sizes
372 and comparing them to the size of waves near the magnetic equator where those
373 electrons could have been scattered. Chapter X describes a microburst scattering
374 event observed by NASA's Van Allen Probes which was studied in the theoretic
375 framework of pitch angle and energy diffusion. The following two chapters will then
376 study the size of microbursts. Chapter Y describes a bouncing packet microburst
377 observation made by MSU's FIREBIRD-II mission where the microburst's lower
378 bound longitudinal and latitudinal sizes were estimated. Then Chapter Z expands
379 the case study from Ch. Y to a statistical study of microburst sizes using The
380 Aerospace Corporation's AeroCube-6 (AC6) CubeSats. In this study, a Monte Carlo
381 and analytic microburst size models were developed to account for the compounding
382 effects of random microburst sizes and locations. Lastly, Ch. A will summarize the
383 dissertation work and make concluding remarks regarding outstanding questions in
384 microburst physics.

Bibliography

- 386 Anderson, B., Shekhar, S., Millan, R., Crew, A., Spence, H., Klumpar, D., Blake, J.,
 387 O'Brien, T., and Turner, D. (2017). Spatial scale and duration of one microburst
 388 region on 13 August 2015. *Journal of Geophysical Research: Space Physics*.
- 389 Anderson, K. A. and Milton, D. W. (1964). Balloon observations of X rays in the
 390 auroral zone: 3. High time resolution studies. *Journal of Geophysical Research*,
 391 69(21):4457–4479.
- 392 Barcus, J., Brown, R., and Rosenberg, T. (1966). Spatial and temporal character of
 393 fast variations in auroral-zone x rays. *Journal of Geophysical Research*, 71(1):125–
 394 141.
- 395 Baumjohann, W. and Treumann, R. A. (1997). *Basic space plasma physics*. World
 396 Scientific.
- 397 Blake, J.,Looper, M., Baker, D., Nakamura, R., Klecker, B., and Hovestadt, D.
 398 (1996). New high temporal and spatial resolution measurements by sampex of the
 399 precipitation of relativistic electrons. *Advances in Space Research*, 18(8):171 – 186.
- 400 Blake, J. B. and O'Brien, T. P. (2016). Observations of small-scale latitudinal
 401 structure in energetic electron precipitation. *Journal of Geophysical Research: Space
 402 Physics*, 121(4):3031–3035. 2015JA021815.
- 403 Blum, L., Li, X., and Denton, M. (2015). Rapid MeV electron precipitation as
 404 observed by SAMPEX/HILT during high-speed stream-driven storms. *Journal of
 405 Geophysical Research: Space Physics*, 120(5):3783–3794. 2014JA020633.
- 406 Breneman, A., Crew, A., Sample, J., Klumpar, D., Johnson, A., Agapitov, O.,
 407 Shumko, M., Turner, D., Santolik, O., Wygant, J., et al. (2017). Observations
 408 directly linking relativistic electron microbursts to whistler mode chorus: Van allen
 409 probes and FIREBIRD II. *Geophysical Research Letters*.
- 410 Breneman, A. W., Halford, A., Millan, R., McCarthy, M., Fennell, J., Sample, J.,
 411 Woodger, L., Hospodarsky, G., Wygant, J. R., Cattell, C. A., et al. (2015). Global-
 412 scale coherence modulation of radiation-belt electron loss from plasmaspheric hiss.
 413 *Nature*, 523(7559):193.
- 414 Brown, R., Barcus, J., and Parsons, N. (1965). Balloon observations of auroral zone
 415 x rays in conjugate regions. 2. microbursts and pulsations. *Journal of Geophysical
 416 Research (U.S.)*.
- 417 Capannolo, L., Li, W., Ma, Q., Shen, X.-C., Zhang, X.-J., Redmon, R., Rodriguez,
 418 J., Engebretson, M., Kletzing, C., Kurth, W., et al. (2019). Energetic electron
 419 precipitation: multi-event analysis of its spatial extent during emic wave activity.
 420 *Journal of Geophysical Research: Space Physics*.

- 421 Claudepierre, S., O'Brien, T.,Looper, M., Blake, J., Fennell, J., Roeder, J.,
 422 Clemmons, J., Mazur, J., Turner, D., Reeves, G., et al. (2019). A revised look
 423 at relativistic electrons in the earth's inner radiation zone and slot region. *Journal*
 424 *of Geophysical Research: Space Physics*, 124(2):934–951.
- 425 Crew, A. B., Spence, H. E., Blake, J. B., Klumpar, D. M., Larsen, B. A., O'Brien,
 426 T. P., Driscoll, S., Handley, M., Legere, J., Longworth, S., Mashburn, K.,
 427 Mosleh, E., Ryhajlo, N., Smith, S., Springer, L., and Widholm, M. (2016). First
 428 multipoint in situ observations of electron microbursts: Initial results from the
 429 NSF FIREBIRD II mission. *Journal of Geophysical Research: Space Physics*,
 430 121(6):5272–5283. 2016JA022485.
- 431 Datta, S., Skoug, R., McCarthy, M., and Parks, G. (1997). Modeling of microburst
 432 electron precipitation using pitch angle diffusion theory. *Journal of Geophysical*
 433 *Research: Space Physics*, 102(A8):17325–17333.
- 434 Douma, E., Rodger, C. J., Blum, L. W., and Clilverd, M. A. (2017). Occurrence
 435 characteristics of relativistic electron microbursts from SAMPEX observations.
 436 *Journal of Geophysical Research: Space Physics*, 122(8):8096–8107. 2017JA024067.
- 437 Dungey, J. W. (1961). Interplanetary magnetic field and the auroral zones. *Phys.*
 438 *Rev. Lett.*, 6:47–48.
- 439 Greeley, A., Kanekal, S., Baker, D., Klecker, B., and Schiller, Q. (2019). Quantifying
 440 the contribution of microbursts to global electron loss in the radiation belts. *Journal*
 441 *of Geophysical Research: Space Physics*.
- 442 Hendry, A. T., Rodger, C. J., and Clilverd, M. A. (2017). Evidence of sub-mev
 443 emic-driven electron precipitation. *Geophysical Research Letters*, 44(3):1210–1218.
- 444 Horne, R., Glauert, S., Meredith, N., Boscher, D., Maget, V., Heynderickx, D., and
 445 Pitchford, D. (2013). Space weather impacts on satellites and forecasting the earth's
 446 electron radiation belts with spacecast. *Space Weather*, 11(4):169–186.
- 447 Horne, R. B., Thorne, R. M., Shprits, Y. Y., Meredith, N. P., Glauert, S. A., Smith,
 448 A. J., Kanekal, S. G., Baker, D. N., Engebretson, M. J., Posch, J. L., et al.
 449 (2005). Wave acceleration of electrons in the van allen radiation belts. *Nature*,
 450 437(7056):227.
- 451 Kasahara, S., Miyoshi, Y., Yokota, S., Mitani, T., Kasahara, Y., Matsuda, S.,
 452 Kumamoto, A., Matsuoka, A., Kazama, Y., Frey, H., et al. (2018). Pulsating
 453 aurora from electron scattering by chorus waves. *Nature*, 554(7692):337.
- 454 Lee, J. J., Parks, G. K., Lee, E., Tsurutani, B. T., Hwang, J., Cho, K. S., Kim, K.-H.,
 455 Park, Y. D., Min, K. W., and McCarthy, M. P. (2012). Anisotropic pitch angle
 456 distribution of 100 keV microburst electrons in the loss cone: measurements from
 457 STSAT-1. *Annales Geophysicae*, 30(11):1567–1573.

- 458 Lee, J.-J., Parks, G. K., Min, K. W., Kim, H. J., Park, J., Hwang, J., McCarthy,
 459 M. P., Lee, E., Ryu, K. S., Lim, J. T., Sim, E. S., Lee, H. W., Kang, K. I., and
 460 Park, H. Y. (2005). Energy spectra of 170–360 keV electron microbursts measured
 461 by the korean STSAT-1. *Geophysical Research Letters*, 32(13). L13106.
- 462 Li, X., Selesnick, R., Schiller, Q., Zhang, K., Zhao, H., Baker, D. N., and Temerin,
 463 M. A. (2017). Measurement of electrons from albedo neutron decay and neutron
 464 density in near-earth space. *Nature*, 552(7685):382.
- 465 Lorentzen, K. R., Blake, J. B., Inan, U. S., and Bortnik, J. (2001a). Observations
 466 of relativistic electron microbursts in association with VLF chorus. *Journal of
 467 Geophysical Research: Space Physics*, 106(A4):6017–6027.
- 468 Lorentzen, K. R.,Looper, M. D., and Blake, J. B. (2001b). Relativistic electron
 469 microbursts during the GEM storms. *Geophysical Research Letters*, 28(13):2573–
 470 2576.
- 471 Lyons, L. R. and Thorne, R. M. (1973). Equilibrium structure of radiation belt
 472 electrons. *Journal of Geophysical Research*, 78(13):2142–2149.
- 473 Millan, R. and Thorne, R. (2007). Review of radiation belt relativistic electron losses.
 474 *Journal of Atmospheric and Solar-Terrestrial Physics*, 69(3):362 – 377.
- 475 Nakamura, R., Baker, D. N., Blake, J. B., Kanekal, S., Klecker, B., and Hovestadt,
 476 D. (1995). Relativistic electron precipitation enhancements near the outer edge of
 477 the radiation belt. *Geophysical Research Letters*, 22(9):1129–1132.
- 478 Nakamura, R., Isowa, M., Kamide, Y., Baker, D., Blake, J., and Looper, M. (2000).
 479 Observations of relativistic electron microbursts in association with VLF chorus.
 480 *J. Geophys. Res*, 105:15875–15885.
- 481 O'Brien, T., Claudepierre, S., Blake, J., Fennell, J. F., Clemons, J., Roeder, J.,
 482 Spence, H. E., Reeves, G., and Baker, D. (2014). An empirically observed pitch-
 483 angle diffusion eigenmode in the earth's electron belt near $l^* = 5.0$. *Geophysical
 484 Research Letters*, 41(2):251–258.
- 485 O'Brien, T., Claudepierre, S., Guild, T., Fennell, J., Turner, D., Blake, J., Clemons,
 486 J., and Roeder, J. (2016). Inner zone and slot electron radial diffusion revisited.
 487 *Geophysical Research Letters*, 43(14):7301–7310.
- 488 O'Brien, T. and Moldwin, M. (2003). Empirical plasmapause models from magnetic
 489 indices. *Geophysical Research Letters*, 30(4).
- 490 O'Brien, T. P., Looper, M. D., and Blake, J. B. (2004). Quantification of relativistic
 491 electron microburst losses during the GEM storms. *Geophysical Research Letters*,
 492 31(4). L04802.

- 493 O'Brien, T. P., Lorentzen, K. R., Mann, I. R., Meredith, N. P., Blake, J. B., Fennell,
 494 J. F., Looper, M. D., Milling, D. K., and Anderson, R. R. (2003). Energization of
 495 relativistic electrons in the presence of ULF power and MeV microbursts: Evidence
 496 for dual ULF and VLF acceleration. *Journal of Geophysical Research: Space
 497 Physics*, 108(A8).
- 498 Ozaki, M., Miyoshi, Y., Shiokawa, K., Hosokawa, K., Oyama, S.-i., Kataoka, R.,
 499 Ebihara, Y., Ogawa, Y., Kasahara, Y., Yagitani, S., et al. (2019). Visualization of
 500 rapid electron precipitation via chorus element wave-particle interactions. *Nature
 501 communications*, 10(1):257.
- 502 Parks, G. K. (1967). Spatial characteristics of auroral-zone X-ray microbursts. *Journal
 503 of Geophysical Research*, 72(1):215–226.
- 504 Reeves, G., Spence, H. E., Henderson, M., Morley, S., Friedel, R., Funsten, H., Baker,
 505 D., Kanekal, S., Blake, J., Fennell, J., et al. (2013). Electron acceleration in the
 506 heart of the van allen radiation belts. *Science*, 341(6149):991–994.
- 507 Reeves, G. D., McAdams, K. L., Friedel, R. H. W., and O'Brien, T. P. (2003). Ac-
 508 celeration and loss of relativistic electrons during geomagnetic storms. *Geophysical
 509 Research Letters*, 30(10):n/a–n/a. 1529.
- 510 Schulz, M. and Lanzerotti, L. J. (1974). *Particle Diffusion in the Radiation Belts*.
 511 Springer.
- 512 Trefall, H., Bjordal, J., Ullaland, S., and Stadsnes, J. (1966). On the extension of
 513 auroral-zone x-ray microbursts. *Journal of Atmospheric and Terrestrial Physics*,
 514 28(2):225–233.
- 515 Tsurutani, B. T. and Lakhina, G. S. (1997). Some basic concepts of wave-particle
 516 interactions in collisionless plasmas. *Reviews of Geophysics*, 35(4):491–501.
- 517 Turner, D., Claudepierre, S., Fennell, J., O'Brien, T., Blake, J., Lemon, C.,
 518 Gkioulidou, M., Takahashi, K., Reeves, G., Thaller, S., et al. (2015). Energetic
 519 electron injections deep into the inner magnetosphere associated with substorm
 520 activity. *Geophysical Research Letters*, 42(7):2079–2087.
- 521 Ukhorskiy, A. Y., Anderson, B. J., Brandt, P. C., and Tsyganenko, N. A. (2006).
 522 Storm time evolution of the outer radiation belt: Transport and losses. *Journal of
 523 Geophysical Research: Space Physics*, 111(A11):n/a–n/a. A11S03.
- 524 Van Allen, J. A. (1959). The geomagnetically trapped corpuscular radiation. *Journal
 525 of Geophysical Research*, 64(11):1683–1689.
- 526 Vernov, S. and Chudakov, A. (1960). Investigation of radiation in outer space. In
 527 *International Cosmic Ray Conference*, volume 3, page 19.

- 528 Woodger, L., Halford, A., Millan, R., McCarthy, M., Smith, D., Bowers, G., Sample,
529 J., Anderson, B., and Liang, X. (2015). A summary of the BARREL campaigns:
530 Technique for studying electron precipitation. *Journal of Geophysical Research: Space Physics*, 120(6):4922–4935.
531